Imaging Spatiotemporal Hong-Ou-Mandel Interference of Biphoton States of Extremely High Schmidt Number

Fabrice Devaux,[1,*] Alexis Mosset,[1] Paul-Antoine Moreau,[2] and Eric Lantz[1]

[1]*Institut FEMTO-ST, Département d'Optique P. M. Duffieux, UMR 6174 CNRS Université Bourgogne Franche-Comté, 15b Avenue des Montboucons, 25030 Besançon, France*

[2]*School of Physics and Astronomy, University of Glasgow, G12 8QQ, United Kingdom*

(Received 18 February 2020; revised 17 April 2020; accepted 11 June 2020; published 11 August 2020)

We report the experimental observation of a spatiotemporal Hong-Ou-Mandel (HOM) interference of biphoton states of extremely high Schmidt number. Two-photon interference of 1500 spatial modes and a total of more than 3×10^6 spatiotemporal modes is evidenced by measuring momentum spatial coincidences, without any prior selection of the photons in time and space coincidence, between the pixels of the far-field images of two strongly multimode spontaneous parametric down-conversion (SPDC) beams propagating through a HOM interferometer. The outgoing SPDC beams are recorded on two separate detector arrays operating in the photon-counting regime. The properties of HOM interference are investigated both in the time and space domains. We show that the two-photon interference exhibits temporal and two-dimensional spatial HOM dips with visibilities of 60% and widths in good agreement with the spatiotemporal coherence properties of the biphoton state. Moreover, we demonstrate that maxima of momentum spatial coincidences are evidenced within each image, in correspondence with these dips.

DOI: 10.1103/PhysRevX.10.031031 Subject Areas: Optics, Photonics, Quantum Physics

I. INTRODUCTION

Spatial entanglement of photon pairs in images offers new opportunities to develop protocols for communication and parallel treatment of quantum information of potentially very high dimensionality. Although entangled photon pairs of high Schmidt number are easily produced by spontaneous parametric down-conversion (SPDC), the manipulation and the detection of images with quantum features is tricky. Fortunately, detector arrays with high sensitivity such as the electron multiplying charge-coupled device (EMCCD), the intensified charge-coupled device (iCCD), or the single photon avalanche diode (SPAD) array [1] are now widely used for quantum imaging experiments [2], like demonstration of the Einstein-Podolsky-Rosen (EPR) paradox in twin images [3–5], imaging of high-dimensional spatial entanglement [6], ghost imaging [7,8], quantum adaptive optics [9], quantum holography [10], sub-shot-noise imaging [11,12], and quantum imaging with undetected photons [13].

Among the whole experiments using entangled pairs of photons, the famous experiment of two-photon interference, now known as Hong-Ou-Mandel (HOM) interference [14], is probably one of the most fascinating. This groundbreaking experiment paved the way for a multitude of experiments showing the richness of the quantum properties of light and their application to original communication protocols [15], to quantum teleportation [16], and in the context of quantum information and computation, e.g., in linear optical quantum computing [17] and, more particularly, in boson sampling [18]. Most of these experiments and protocols used the coherence time properties of the biphoton state, and the measurements are performed by means of bucket detectors and coincidence counters gated in time. HOM interference is obtained if the two photons involved are indistinguishable, whatever their origin, meaning that extremely dissimilar light sources [19] can be used if the corresponding modes are thoroughly tailored. On the other hand, genuine multimode HOM interference implies entanglement, as quoted by Lee *et al.* [20], and SPDC remains the simplest way to produce entangled photon pairs of high dimensionality. Recently, Jachura *et al.* [21] extended the applications of the camera systems to the observation of HOM interference with an intensified scientific complementary metal-oxide-semiconductor (sCMOS) camera, showing a maximum of coincidences on the same region of interest (ROI) of the camera in conditions corresponding to a minimum of the dip between separate ROIs of the camera. Nevertheless, the input photons were spatially filtered by traversing a single-mode fiber to ensure a unique input spatial mode for each photon. It is possible to imprint a phase profile on one of the photons and to realize its hologram, as demonstrated by the

*Corresponding author.
fabrice.devaux@univ-fcomte.fr

same group [22]. Also in this experiment, only a spatial mode per input port is involved, even if shaped. In the experiments reported in Refs. [23,24], it was shown that a tilt between the spatially monomode input beams results in coincidence fringes that were detected by scanning a bucket detector. On the other hand, two experiments demonstrated multimode HOM interference. First, Walborn *et al.* [25] showed that a HOM dip can be transformed in a HOM peak by using either an antisymmetric pump beam or an antisymmetric polarization vector of the entangled photon pair. Second, Lee *et al.* employed bucket detectors and time coincidence to characterize HOM interference from SPDC limited by an aperture [20] or whose orbital angular momentum (OAM) has been modified by an image rotator [26], resulting in a maximum of about 40 spatial modes or 20 OAM modes.

Recently, using numerical simulations with realistic parameters, we have shown how two cameras can be used to detect two-dimensional (2D) spatial coincidences of biphoton states of high dimensionality and to evidence HOM interferences between the two outgoing images [27]. Thanks to this numerical model, we have demonstrated that such a HOM interferometer allows the characterization of the temporal as well as the 2D spatial coherence properties of entangled photon pairs.

In this paper, we report the first experimental observation of a fully spatiotemporal HOM interference of biphoton states of high Schmidt number. Two-photon interferences are evidenced by measuring the 2D momentum spatial coincidences between the pixels of far-field images of twin SPDC beams propagating through the HOM interferometer without any prior selection of the photons in time and space coincidence. The images are recorded onto two EMCCDs operating in the photon-counting regime [28]. The use of EMCCDs allows the detection of all photons of the images and the measurement of spatial coincidences on the whole set of photons. The properties of HOM interference are investigated both in the time and space domains, as proposed in Ref. [27]. Given the critical role played by two-photon HOM interferences in most quantum information and quantum technology schemes, our demonstration that HOM interference can be obtained by manipulating a very-high-dimensional entangled state paves the way to very-high-dimensional quantum information schemes using space and time variables.

II. EXPERIMENTAL SETUP AND METHOD

Figure 1(a) shows the experimental setup that closely corresponds to the setup modelized in Ref. [27]. Strongly multimode twin SPDC beams (i.e., biphoton states of high Schmidt number) are generated in a noncollinear type-II geometry in a 0.8-mm-long β-barium borate (β-BBO) crystal pumped at 355 nm. The pump pulses are provided by a passively Q-switched Nd:YAG laser ($\Delta t_{\mathrm{pump}} = 660$ ps FWHM pulse duration, 8-mW mean power, and 4-kHz repetition rate). Because of the noncollinear interaction, the twin beams are separated and propagate through the two input ports of the HOM interferometer up to a beam splitter (BS: $R = 50\%$, $T = 40\%$, losses 10%). In both arms, two identical 1.5 magnification telescopes form the near-field images of the BBO crystal inside the BS. Because of the geometry of the interferometer [27] where SPDC beams propagate in the horizontal plane, the reflected beams experience a left-right symmetry with respect to the transmitted beams in the near field as well as in the far field. Before the BS, the polarization state of the idler beam is controlled with a half-wave plate (HWP), in order to measure spatial correlations when the polarization states of the twin photons are horizontal-vertical (HV) or vertical-vertical (VV). Then, the far field of the two outgoing images is formed with $2f$ imaging systems on two separate EMCCDs (ANDOR iXon Ultra 897), used in the photon-counting regime [28]. Before detection, the photon pairs emitted around the degeneracy are selected by narrow-band interference filters (IF) centered at 709 nm ($\Delta\lambda_{\mathrm{IF}} \simeq 5$ nm, FWHM bandwidth). Figures 1(b) and 1(c) show typical far-field and near-field average images of the SPDC beams through the HOM interferometer. The axes of the far-field image are graduated in spatial frequency coordinates $\nu_{x,y}$, which are related to momentum coordinates by $q_{x,y} = 2\pi\nu_{x,y}$.

The control (by a delay line) of the time delay δt between the input ports of the HOM interferometer gives access to the coherence length. Meanwhile, the control of a 2D transverse spatial frequency shift between the transmitted and reflected beams at the output ports, by the rotations $\delta\theta_{\mathrm{BS}}$ and $\delta\phi_{\mathrm{BS}}$ of the BS, gives us access to the two transverse coherence widths of the biphoton state. From the far-field and near-field images of the SPDC beams [Figs. 1(b) and 1(c)], the time duration of the pump pulse, and the bandwidth of the IF, we estimate the standard deviations of the SPDC beams in the spatial and temporal domains as

$$\begin{aligned}
&\sigma_x^{\mathrm{SPDC}} \simeq \sigma_x^{\mathrm{pump}} \simeq 0.35 \text{ mm}\\
&\sigma_y^{\mathrm{SPDC}} \simeq \sigma_y^{\mathrm{pump}} \simeq 0.37 \text{ mm}\\
&\sigma_{\nu_x}^{\mathrm{SPDC}} \simeq 34 \text{ mm}^{-1}\\
&\sigma_{\nu_y}^{\mathrm{SPDC}} \simeq 34 \text{ mm}^{-1}\\
&\sigma_t^{\mathrm{SPDC}} \simeq \sigma_t^{\mathrm{pump}} \simeq 400 \text{ ps}\\
&\sigma_{\nu_t}^{\mathrm{SPDC}} \simeq \sigma_{\nu_t}^{\mathrm{IF}} \simeq 1.8 \text{ THz}.
\end{aligned} \tag{1}$$

In the context of entangled twin photons [29], the Schmidt number is given along the dimension i (where $i = x, y, t$) by $K_i = \frac{1}{2}[\sigma_i^{\mathrm{pump}} 2\pi\sigma_{\nu_i}^{\mathrm{SPDC}} + (1/\sigma_i^{\mathrm{pump}} 2\pi\sigma_{\nu_i}^{\mathrm{SPDC}})]$. From the experimental parameters [Eq. (1)], we have estimated the Schmidt numbers for each dimension:

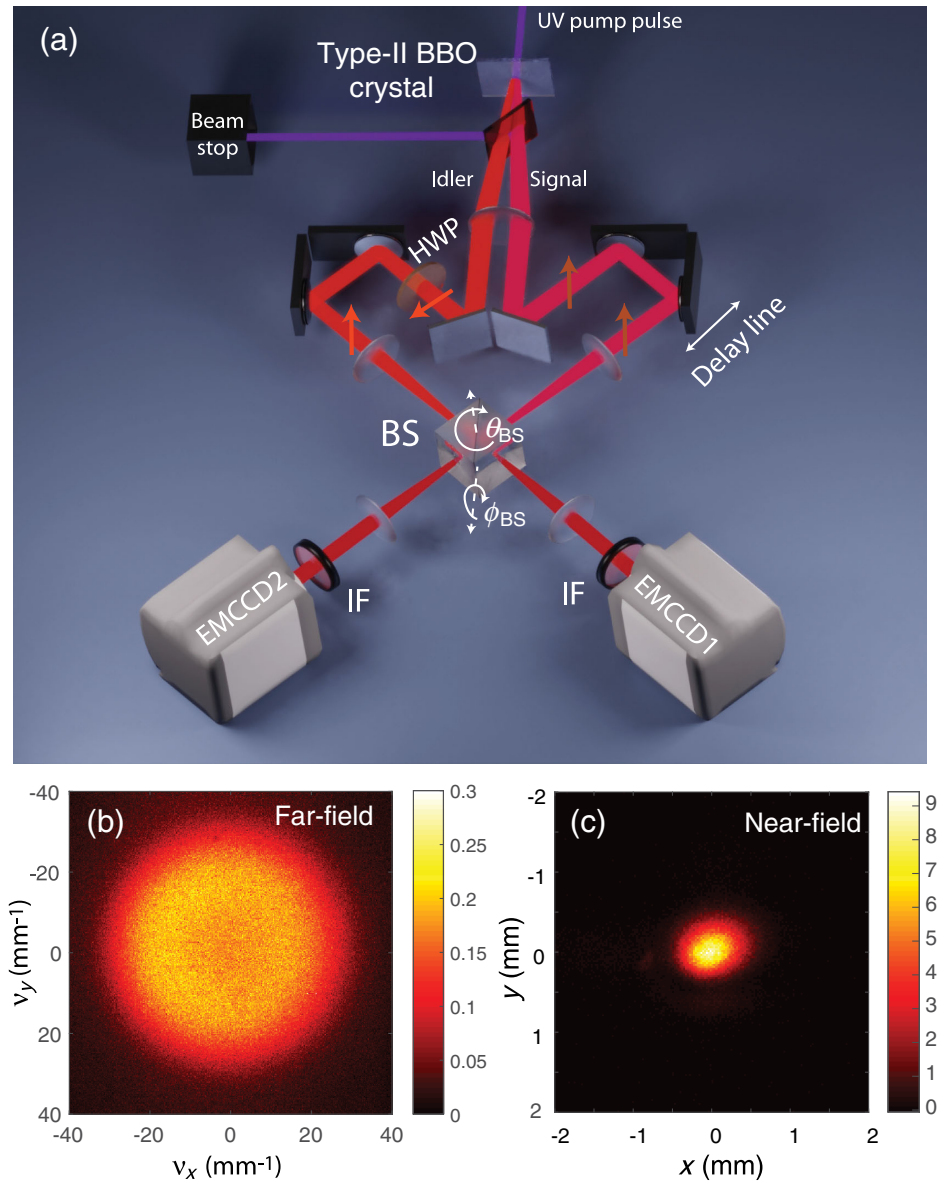

FIG. 1. (a) Experimental setup. (b,c) Average images in photon number of the far field and the near field of a single SPDC beam, respectively.

$$K_x \simeq 37$$
$$K_y \simeq 40$$
$$K_t \simeq 2.3 \times 10^3. \quad (2)$$

Finally, the full space-time dimensionality of the biphoton state can be estimated as $K_x K_y K_t \simeq 3.4 \times 10^6$, which confirms the extremely high dimensionality of the twin photons involved in the HOM interference.

Figures 2(a) and 2(b) schematically illustrate the relative positions and orientations of the far-field patterns of the SPDC beams on both cameras, when they are either transmitted or reflected by the BS. Because of the geometry of the HOM interferometer [27], horizontal and vertical tilts of the BS induce momenta shifts $\boldsymbol{\delta q}$ of the reflected beams, which are related to 2D spatial frequency shifts $\delta\nu_{x_i} = \delta\nu_{x_s} = 2f\delta\theta_{\mathrm{BS}}$ and $\delta\nu_{y_i} = -\delta\nu_{y_s} = 2f\delta\phi_{\mathrm{BS}}$, where f is the focal length of the last lenses before the EMCCDs. Using detector arrays, the momentum spatial correlations between the photons of a pair can be measured between images for transmitted-transmitted (tt) and reflected-reflected (rr) twin photons and also within single images for reflected-transmitted (rt) and transmitted-reflected (tr) twin photons. These different kinds of spatial correlations can be observed by comparing Figs. 2(a) and 2(c) and Figs. 2(b) and 2(e) for correlations within single images and by comparing Figs. 2(a) and 2(d) for correlations between images.

First, let us consider the case where the transmitted and reflected beams are perfectly superimposed on both cameras ($\boldsymbol{\delta q} = \mathbf{0}$), perfectly synchronized ($\delta t = 0$), and

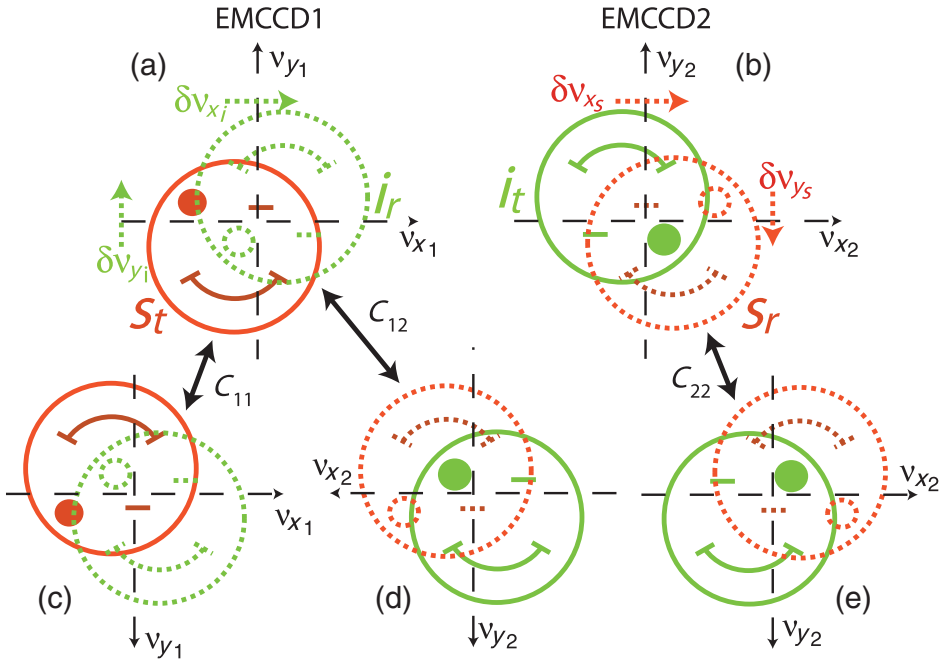

FIG. 2. (a,b) Diagrams illustrating, on both cameras, the relative positions of the far-field patterns of the signal and idler beams, represented in red and green, respectively, when they are either transmitted (s_t, i_t) or reflected (s_r, i_r) as a function of the shifts $\delta\nu_{x_i} = \delta\nu_{x_s}$ and $\delta\nu_{y_i} = -\delta\nu_{y_s}$ induced by horizontal and vertical tilts of the BS, respectively. The solid and dotted circles correspond to the transmitted beams and to the reflected beams, respectively. The origins of the axes are centered on the barycenters of the images. (c,e) Up-down flip applied to images (a) and (b). (d) Left-right and up-down flips applied to image (b). Spatial correlations can be observed within images symmetrically to the horizontal axes (C_{11} and C_{22}) and between images symmetrically to the image barycenters (C_{12}).

parallely polarized (VV configuration). For both reflected (rr) and transmitted beams (tt), momentum correlations are found between pixels of the two cameras corresponding to opposite transverse momenta coordinates $\boldsymbol{q_1}$ and $\boldsymbol{q_2} = -\boldsymbol{q_1} + \boldsymbol{\Delta q}$, where $\boldsymbol{\Delta q}$ denotes the 2D momentum correlation uncertainty. By calculating the normalized cross-correlation between image 1 and the up-down and left-right symmetric image 2, we obtain the spatial distribution of the momentum correlations as a function of the 2D momentum uncertainty: $C_{12}(\boldsymbol{\Delta q})$. For the rt and tr beams, momentum correlations are found within each image between the pixels that are symmetric with respect to the horizontal axis, corresponding to transverse momenta coordinates (q_{x1}, q_{y1}) and $(q_{x1} + \Delta q_x, -q_{y1} + \Delta q_y)$ for camera 1 and (q_{x2}, q_{y2}) and $(q_{x2} + \Delta q_x, -q_{y2} + \Delta q_y)$ for camera 2. For each image, measurements are performed by calculating the normalized cross-correlation between the upper-half and the up-down symmetric lower-half parts of single images. In that case, we do not perform the correlation calculation on the whole image because the correlations between twin photons detected on the same camera would be counted twice. Then, we obtain the spatial distributions of the momentum correlations within each image as a function of the 2D momentum uncertainty: $C_{11}(\boldsymbol{\Delta q})$ and $C_{22}(\boldsymbol{\Delta q})$. In all cases, the correlation distributions have the shape of 2D Gaussian functions with standard deviations related to the spatial dimensionality of the biphoton state. Now, let us consider the case where a time delay and a momentum shift are imposed. In that case, using the formalism proposed in Refs. [27,14], we can establish the relations that give the spatial distributions of momentum correlations as a function of δt and $\boldsymbol{\delta q}$:

$$
\begin{aligned}
&C_{12}(\boldsymbol{\Delta q}; \delta t, \boldsymbol{\delta q}) \\
&\quad = [R^2 C_0(\boldsymbol{\Delta q} + \boldsymbol{\delta q_x}) + T^2 C_0(\boldsymbol{\Delta q} - \boldsymbol{\delta q_x})] \\
&\qquad \times \left(1 - \frac{2RT}{R^2 + T^2} e^{-(\delta q_x^2/\sigma_q^2)} e^{-(\delta q_y^2/\sigma_{\mathrm{SPDC}}^2)} e^{-(\delta t^2/\sigma_t^2)}\right) \\
&C_{11}(\boldsymbol{\Delta q}; \delta t, \boldsymbol{\delta q}) + C_{22}(\boldsymbol{\Delta q}; \delta t, \boldsymbol{\delta q}) \\
&\quad = RT[C_0(\boldsymbol{\Delta q} + \boldsymbol{\delta q_x}) + C_0(\boldsymbol{\Delta q} - \boldsymbol{\delta q_x})] \\
&\qquad \times (1 + e^{-(\delta q_x^2/\sigma_q^2)} e^{-(\delta q_y^2/\sigma_{\mathrm{SPDC}}^2)} e^{-(\delta t^2/\sigma_t^2)}).
\end{aligned} \tag{3}
$$

Note that $C_0(\boldsymbol{\Delta q})$ is the spatial distribution of momentum correlations measured between twin images when the BS is removed. According to these equations, we should measure two correlation peaks centered along the horizontal axis at a distance related to the horizontal spatial shift and with amplitudes related to the spatial and temporal shifts. As was demonstrated in Ref. [27], the standard deviations of the spatial HOM dip depend of the coherence width of the biphoton wave packet along the horizontal dimension σ_q and of the phase-matching bandwidth σ_{SPDC}

along the vertical dimension. Here, σ_t is the standard deviation of the temporal HOM dip. A 2D space integration of Eq. (3), normalized by a 2D space integration of $C_0(\boldsymbol{\Delta q})$, leads to the relative spatial correlations as a function of the momentum shift and the time delay as follows:

$$R_{12}(\delta t, \boldsymbol{\delta q}) = R^2 + T^2 - 2RTe^{-(\delta q_x^2/\sigma_q^2)}e^{-(\delta q_y^2/\sigma_{\mathrm{SPDC}}^2)}e^{-(\delta t^2/\sigma_t^2)}$$
$$R_{11}(\delta t, \boldsymbol{\delta q}) + R_{22}(\delta t, \boldsymbol{\delta q})$$
$$= 2RT \times (1 + e^{-(\delta q_x^2/\sigma_q^2)}e^{-(\delta q_y^2/\sigma_{\mathrm{SPDC}}^2)}e^{-(\delta t^2/\sigma_t^2)}). \quad (4)$$

Equation (4) clearly shows that when twin photons are indistinguishable, the drop in spatial correlations between the two images (HOM dip) is accompanied by an increase in spatial correlations within the individual images (HOM maximum). Using the definition of the HOM dip visibility [20]: $V_{12} = [(R_{12}^{\max} - R_{12}^{\min})/R_{12}^{\max}] = [2RT/(R^2 + T^2)]$ and defining the visibility of the HOM maximum as $V_{11+22} = \{[(R_{11} + R_{22})_{\max} - (R_{11} + R_{22})\ \min]/[(R_{11} + R_{22})_{\max}]\} = \frac{1}{2}$, visibilities of 98% of the HOM dip and 50% of the HOM maximum are expected, considering the measured values of R and T ($R = 50\%$ and $T = 40\%$).

III. EXPERIMENTAL RESULTS

A. Temporal coherence measurements

The first experiment consists in measuring the temporal coherence of the biphoton state. To this end, the signal and the idler beams are spatially superimposed as precisely as possible in the near-field and far-field domains. Then, spatial-momentum correlations are measured, between pairs of images as well as within single images, as a function of the optical path delay between the two arms of the HOM interferometer and as a function of the polarization states HV and VV of the twin photons. Figure 3 shows the spatial-momentum correlation distributions obtained when they are measured between image pairs (C_{12}) and within single images (C_{11}, C_{22}) and when the time delay between the two arms of the interferometer is null. These results are averaged over 500 pairs of images. Figures 3(a)–3(c) are related to the HV polarization states, and Figs. 3(d)–3(f) are related to the VV polarization states. From these figures, we can observe that the three correlation peaks have the same Gaussian-like shapes, with standard deviations $\sigma_{\nu_x} = 0.8 \pm 0.2\ \mathrm{mm}^{-1}$ and $\sigma_{\nu_y} = 0.6 \pm 0.2\ \mathrm{mm}^{-1}$, which means that spatial-momentum correlations are measured with the same precision between images or within single images. Then, we can roughly estimate the spatial dimensionality of the biphoton state as $[(\sigma_{\nu_x}^{\mathrm{SPDC}}\sigma_{\nu_y}^{\mathrm{SPDC}})/(\sigma_{\nu_x}\sigma_{\nu_x})] = [34^2/(0.8 \times 0.6)] \backsimeq 2400$. This result is of the same order of magnitude as the product of the estimated K_x and K_y Schmidt numbers [Eq. (2)] and confirms the high spatial dimensionality of the biphoton states. By integrating the correlation peaks, we have estimated the ratio of events corresponding to the detection of photons by pairs between images and within single images. When twin photons are cross-polarized (HV), these ratios are $13\% \pm 2\%$ in C_{12} and $7\% \pm 1\%$ in C_{11} and C_{22}. Thus, more or less half of the spatial-momentum coincidences are recorded between the two images, and the

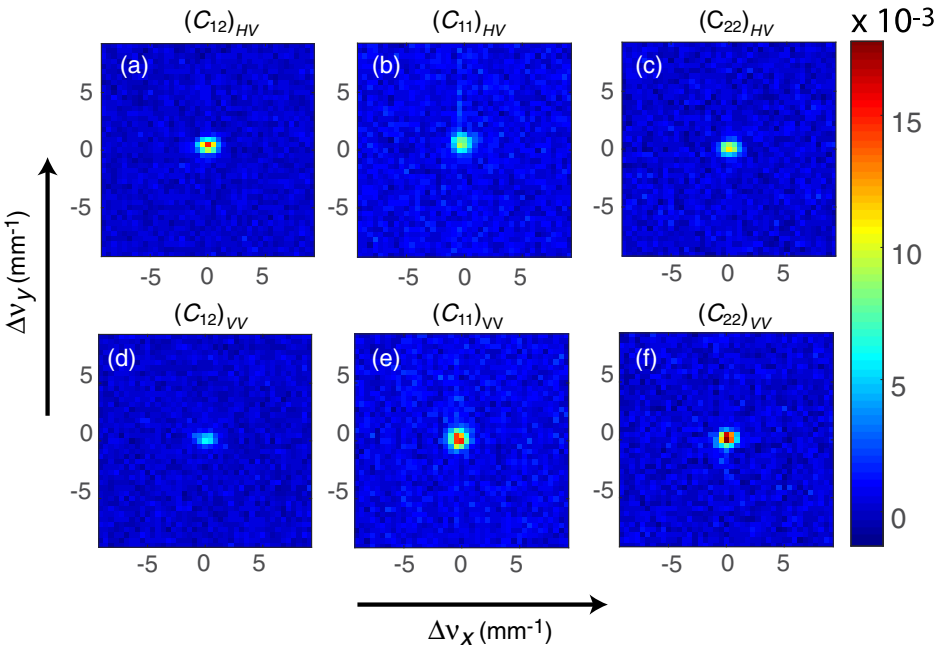

FIG. 3. Average normalized spatial-momentum correlation distributions obtained when correlations are measured between image pairs (C_{12}) and within single images (C_{11}, C_{22}) when the optical path difference between the two arms of the interferometer is null. Note that HV and VV indices are related to the polarization states of the twin photons.

other half are equally distributed within the single images. For the VV polarization states, the ratio in C_{12} decreases to $5\% \pm 1\%$ and increases up to $10\% \pm 1\%$ in C_{11} and $8\% \pm 1\%$ in C_{22}. Consequently, the decrease of the ratio of spatial coincidences between images and its increase within single images clearly demonstrates that a HOM interference occurs for the biphoton state of high Schmidt number. For HV and VV configurations, the sum of the correlation ratios is somewhat smaller than the 25% ratio measured between twin images without the BS, probably because of the losses of the BS.

In order to estimate the coherence length of the biphoton state, we have measured the variation of the relative ratios of total photon-pair detection events in images as a function of the time delay for VV polarization states. These relative ratios [Eq. (4)] correspond to the number of detected photon pairs measured between twin images as well as within single images, divided by the number of detected photon pairs without the BS. Results are depicted in Fig. 4. As expected, while a HOM dip is clearly exhibited for correlations between images, a HOM maximum is observed for correlations within single images. From nonlinear fits, we estimate the visibilities of the HOM dip to $58\% \pm 10\%$ and of the HOM maximum to $34\% \pm 10\%$, which is smaller than the expected visibilities (98% and 50%, respectively). This discrepancy can be due to a number of causes:

(i) the asymmetry of the pump beam [Fig. 1(c)],
(ii) the asymmetry of the SPDC beams at the output of the crystal, because of the walk-off in the crystal,
(iii) the cumulated geometric aberrations in the imaging systems and some residual misalignment,
(iv) some difference in the magnification of the optical systems in both arms.

Of all the causes listed that may reduce the visibility of the HOM interference, geometric aberrations and residual misalignments are probably the main causes. These defects should be corrected by a better control of the alignment procedure. All of these causes have effects on the spatial map of HOM interference (see Fig. 8). Note, however, that this discrepancy cannot be due to the imperfect nature of detectors, whatever its nature, because these detectors are independent. The use of covariances, or correlations after normalization, eliminates the accidental coincidences: A positive covariance corresponds to the probability of detection of a photon pair on both detectors, i.e., imperfect HOM interference.

To conclude this section, we emphasize that we have achieved simultaneous two-photon interference of 1500 spatial modes (i.e., over 1 order of magnitude more than in the work of Lee *et al.* [20]) with 60% visibility. From the nonlinear fits of the experimental data depicted by the dotted curves in Fig. 4, we also estimate the standard deviation of the Gaussian shape of these curves to $\sigma_t = 133.1 \pm 0.2$ fs, which corresponds to a wavelength standard deviation $\sigma_\lambda = (\lambda_{\mathrm{SPDC}}^2/2\pi c\sigma_t) = 2\mathrm{nm}$ ($\lambda_{\mathrm{SPDC}} = 709$ nm), in good agreement with the FWHM bandwidth of the interferential filter. As EMCCD cameras have no temporal resolution, temporal entanglement cannot be measured directly. However, as the width of the temporal HOM dip is related to the coherence time of the biphoton state, we can estimate the temporal Schmidt number as $K_t = \frac{1}{2}(\sigma_t^{\mathrm{pump}}/\sigma_t) = \frac{1}{2}(400 \times 10^{-12}/133 \times 10^{-15}) \simeq 1500$, which is of the same order of magnitude as the estimated temporal Schmidt number [Eq. (2)].

The next experiment consists in measuring the variation of the relative coincidence ratios R_{12} and $R_{11} + R_{22}$ as a function of the angle between the polarization directions of the twin beams, controlled by means of the HWP. These experimental results, depicted in Fig. 5, clearly show the typical modulation of the HOM interference versus the

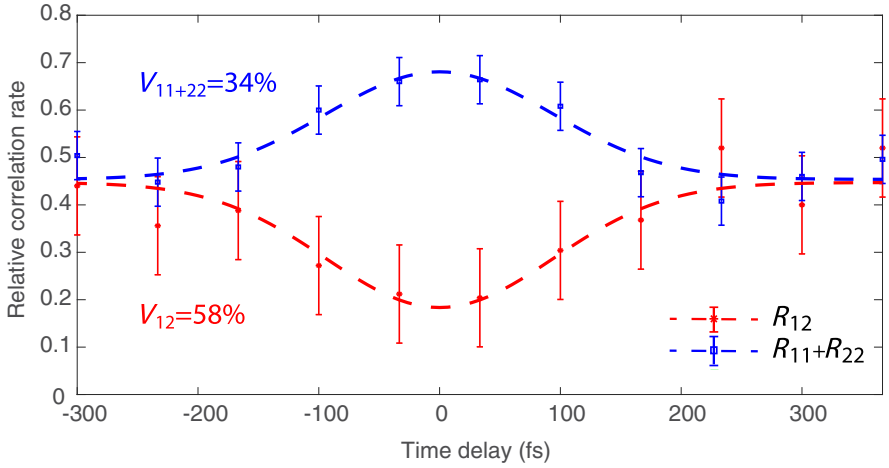

FIG. 4. Relative spatial correlation ratios as a function of the time delay between the two arms of the HOM interferometer when the polarization states of the twin beams are VV. The red stars and blue squares correspond to correlations between twin images and within single images, respectively. The dotted curves correspond to nonlinear fits of the experimental data. These curves exhibit a HOM dip and a HOM maximum with visibilities of 58% and 34%, respectively.

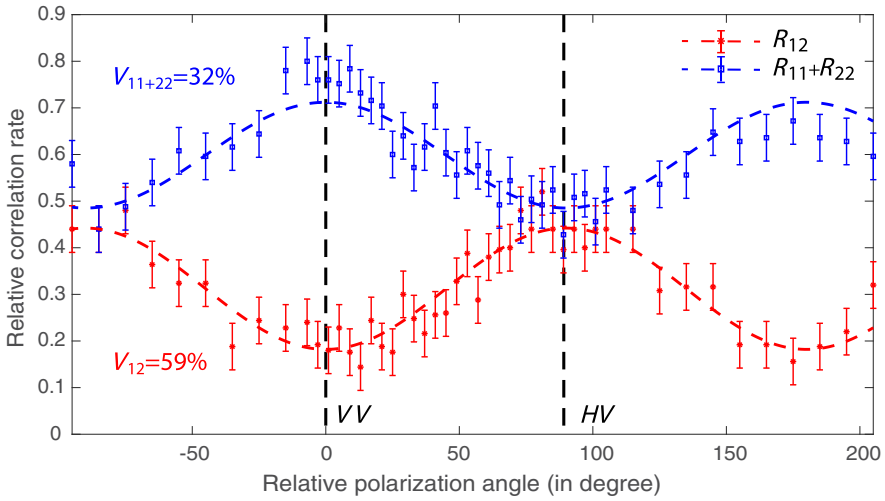

FIG. 5. Correlation ratios as a function of the polarization angle between the two SPDC beams. Red stars and blue squares correspond, respectively, to correlations between the two images (R_{12}) and within single images ($R_{11} + R_{22}$). The dotted curves correspond to nonlinear fits of the experimental data.

relative polarization directions of the twin photons with visibilities $V_{12} = 59\% \pm 10\%$ and $V_{11+22} = 32\% \pm 10\%$, respectively.

B. Spatial coherence measurements

To measure the 2D spatial coherence of the biphoton state, the polarization states of the SPDC beams and the time delay are adjusted to obtain the best polarization and temporal indiscernability of the twin photons. From this initial configuration, vertical and horizontal shifts ($\delta\nu_y$, $\delta\nu_x$) between the reflected and transmitted beams are induced by tilting the BS around its horizontal and vertical axes, respectively (Fig. 1). Then, the variation of the relative spatial correlation ratios between the twin images and within single images is measured as a function of the spatial frequency shifts. These experimental results are given in Figs. 6 and 7.

In Fig. 6, we present images of the 2D momentum correlation distributions $C_{12}(\Delta\boldsymbol{q})$, $C_{11}(\Delta\boldsymbol{q})$, and $C_{22}(\Delta\boldsymbol{q})$ for three different values of the vertical spatial frequency shift: $\delta\nu_y = -4.75$, 0, and $+3.25$ mm^{-1} [Figs. 6(b) to 6(j)]. As was predicted in Ref. [27], single spatial correlation peaks are observed, and their positions do not depend on the vertical spatial shift of the reflected beam. Indeed, because of the geometry of the imaging system, vertical shifts of the reflected beams are in opposite directions on each camera (Fig. 2). Consequently, the spatial-momentum correlations C_{12} between transmitted-transmitted or reflected-reflected twin photons occur between opposite pixels of the twin images with no shift of the symmetry center. Similarly, the spatial-momentum correlations C_{11} and C_{22} between transmitted-reflected or reflected-transmitted twin photons are measured between symmetric pixels along the vertical axis within single images of both cameras, also with the same symmetry center. In that case, the effect of the vertical shift only results in a variation of the relative total number of spatial coincidences between images and within single images [Fig. 6(a)], where R_{12} exhibits a spatial HOM dip and where $R_{11} + R_{22}$ exhibits a HOM maximum with visibilities $V_{12} = 60\% \pm 10\%$ and $V_{11+22} = 39\% \pm 10\%$, respectively. From these curves, we estimate the standard deviation of the dip, versus a vertical frequency shift $\delta\nu_y$ induced by the rotation $\delta\phi_{\mathrm{BS}}$ of the BS, to 2.7 ± 0.3 mm^{-1}, which is larger than the standard deviation of the correlation peaks in the far-field images along the vertical direction, i.e., versus the pixel coordinate $\Delta\nu_y$. According to the geometry of the HOM interferometer, the width of the spatial HOM dip along the vertical direction should be limited by the spatial phase-matching bandwidth [Eq. (4)] for perfect focusing. However, we have demonstrated in Ref. [27] that a small defocusing between image planes reduces the vertical width of the HOM dip. As a perfect superposition of the image planes is experimentally difficult to achieve because of the geometric aberrations of the imaging systems, the measured standard deviation of the HOM dip along the vertical axis is, in agreement with our previous numerical results, smaller than the phase-matching bandwidth and greater than the coherence width of the biphoton state.

In Fig. 7, we present the spatial-momentum correlation distributions for three different values of the horizontal spatial frequency shift: $\delta\nu_x = \pm 2$ and 0 mm^{-1} [Figs. 7(b) to 7(j)]. Contrary to the results for a vertical shift and in good agreement with Ref. [27], the spatial-momentum correlation distributions exhibit two correlation peaks centered at $\pm\delta\nu_x$. In C_{12}, when $\delta\nu_x \neq 0$, the more intense peak corresponds to the *rr* twin photons, and the other peak corresponds to the *tt* twin photons. Indeed, the amplitude difference between the two correlation peaks is due to the difference between the reflection and transmission

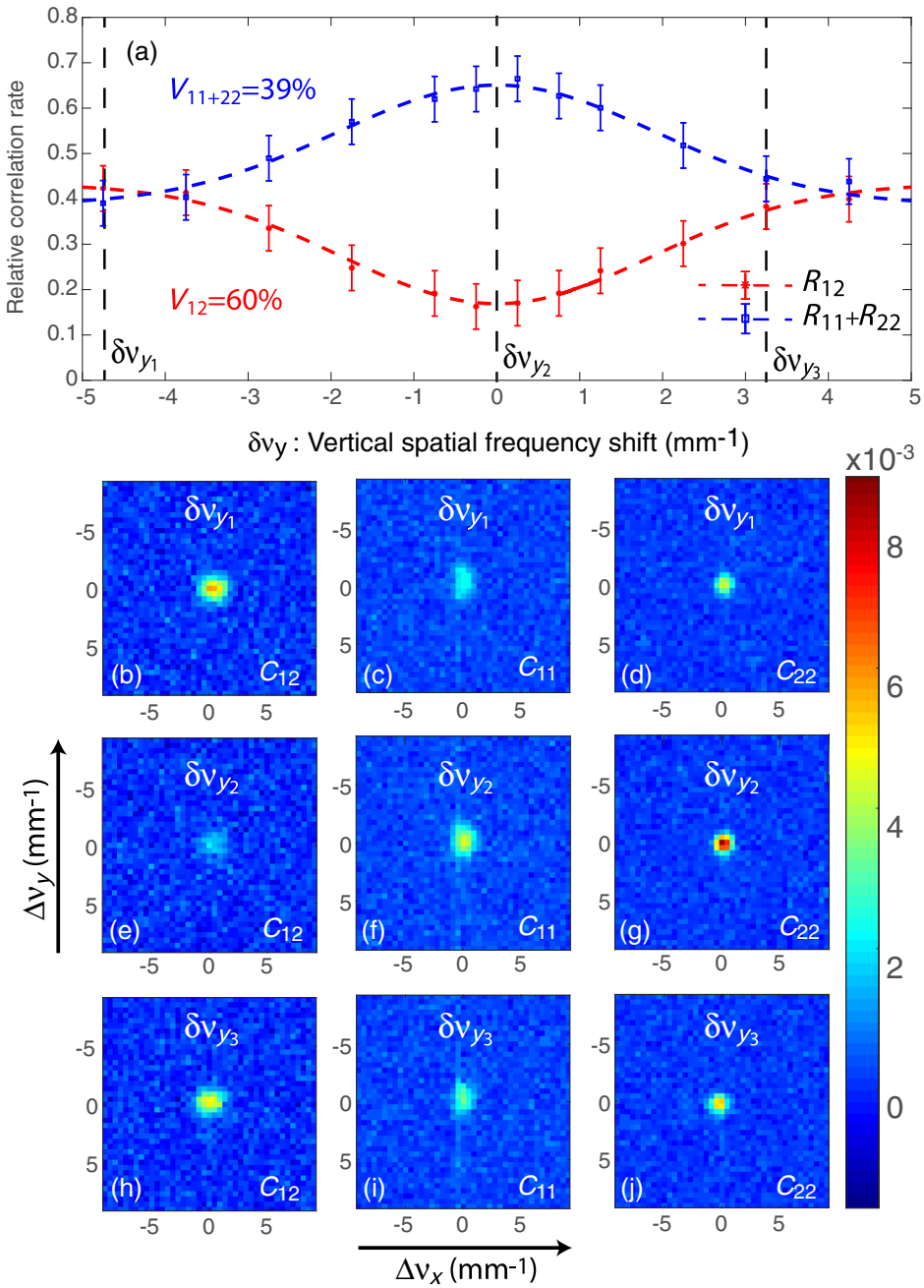

FIG. 6. (a) Relative correlation ratios as a function of the vertical spatial frequency shift $\delta\nu_y$. (b)–(j) Average normalized spatial-momentum correlation distributions C_{12}, C_{11}, and C_{22} for different values of the vertical shift.

coefficients ($R > T$). Moreover, the distance between the two correlation peaks corresponds to $2\delta\nu_x$. For C_{11} and C_{22}, the two correlation peaks are of the same intensity because correlations are calculated between the upper and the lower parts of images where the transmitted and the reflected photons are equally distributed over the area of the detectors. Figure 7(a) shows the variation of the relative total number of spatial coincidences between images and within single images as a function of $\delta\nu_x$, where R_{12} exhibits a spatial HOM dip and where $R_{11} + R_{22}$ exhibits a HOM maximum with visibilities $V_{12} = 63\% \pm 10\%$ and $V_{11+22} = 41\% \pm 10\%$, respectively. From these curves, we estimate the standard deviations of the dip to 0.7 ± 0.1 mm^{-1}, in good agreement with the standard deviation of the correlation peak along the horizontal direction. Figures 6(a) and 7(a) show vertical and horizontal cross sections of the 2D HOM dip and HOM maximum. Two-dimensional mapping of the HOM dip [like in Figs. 5(a) and 6 in Ref. [27]] requires a high degree of accuracy for the spatial frequency scanning and stability of the setup during the necessarily long acquisition time. These conditions have not yet been fulfilled in our setup.

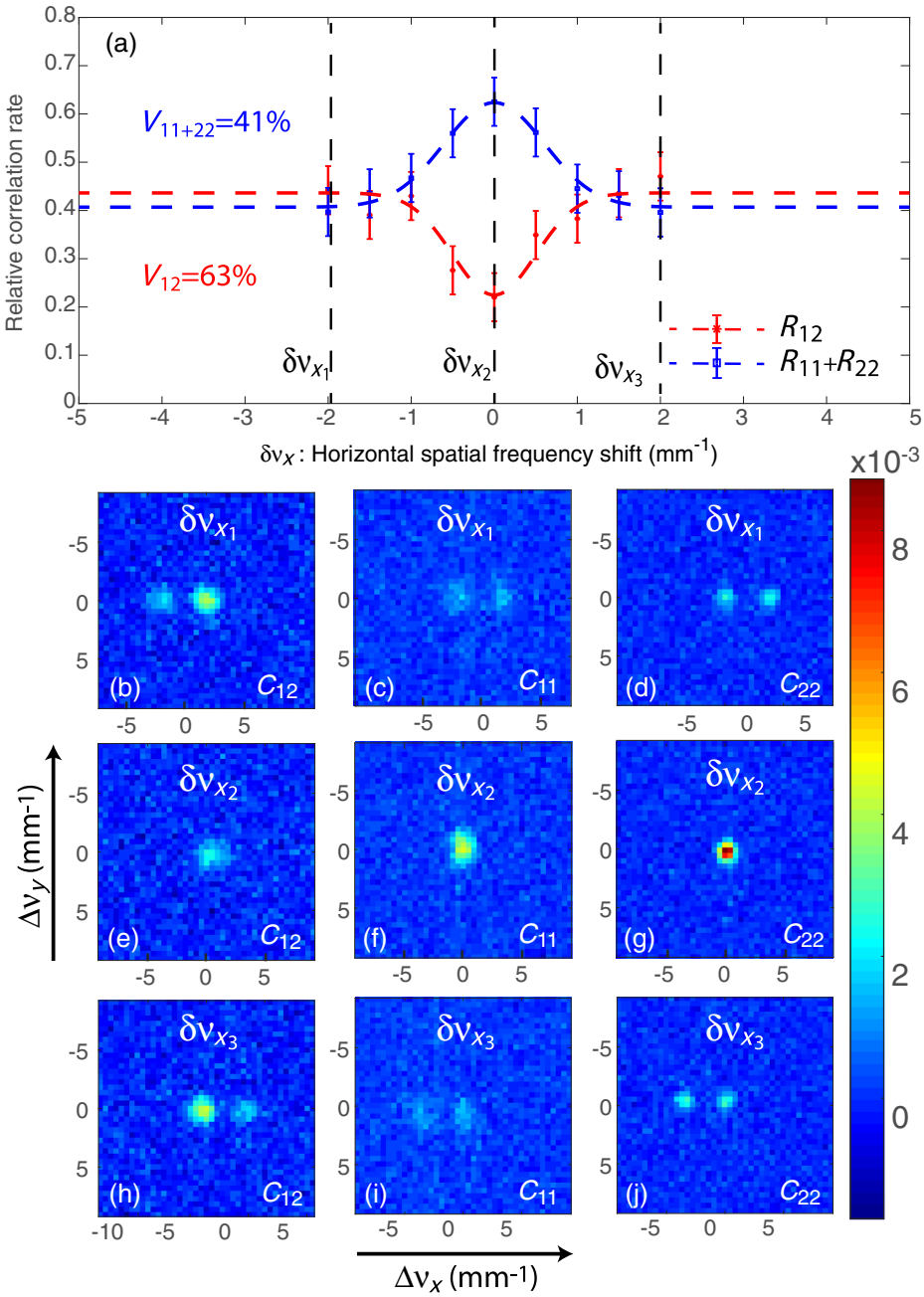

FIG. 7. (a) Relative correlation ratios as a function of the horizontal spatial frequency shift $\delta\nu_x$. (b)–(j) Average normalized spatial-momentum correlation distributions C_{12}, C_{11}, and C_{22} for different values of the horizontal shift.

Among the different improvements of the experimental setup to increase the visibility of the HOM interference, more accurate and automated scanning of the BS should allow us to obtain a 2D map of the HOM dip with good resolution.

Finally, we present in Figs. 8(a)–8(f) the average correlation maps of the intensity fluctuations calculated between 4×4 binned pixels of 500 twin SPDC images versus 1D and 2D spatial transverse coordinates q_x and q_y (given in pixels), for crossed (HV) and parallel (VV) polarizations, when the twin beams are spatially and temporally superimposed ($\boldsymbol{\delta q} = \mathbf{0}$, $\delta t = 0$, Fig. 3). While the 1D maps give the classical representation of 1D far-field spatial correlations between twin photons, Figs. 8(c) and 8(f) show a first tentative of 2D resolution of the spatial coincidences between twin photons in the whole SPDC beam cross section. Figure 8(g) shows the same 2D map obtained with a set of two images issued from two different laser shots. Amplitudes of these maps are normalized by the maximum of the 2D correlation map

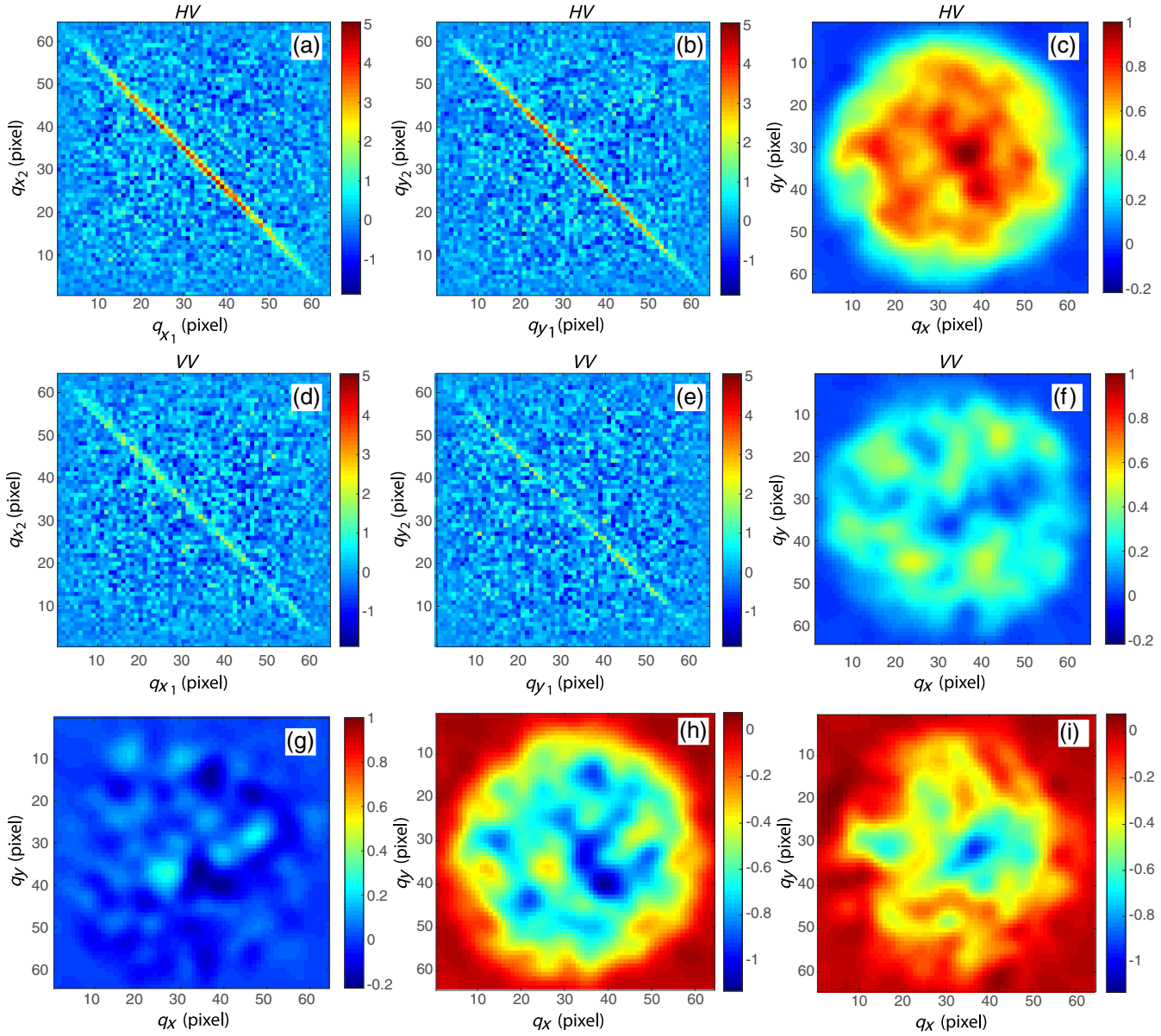

FIG. 8. (a)–(f) Average covariance maps of the intensity fluctuations between pixels of 500 twin SPDC images versus 1D and 2D spatial transverse coordinates q_x and q_y, for crossed (HV) or parallel (VV) polarizations. (g) Covariance map of the intensity fluctuations between pixels of 500 independent SPDC images versus 2D spatial transverse coordinates, normalized by the maximum covariance for HV polarization. (h) Difference between the covariance maps (g) and (c). (i) Difference between the covariance maps (f) and (c).

corresponding to the HV configuration [Fig. 8(c)]. From these 2D maps, we have calculated the spatial distribution of the fall of coincidences between the HV and VV maps [Fig. 8(i)] and the fall obtained when correlating two images issued from two different laser shots [Fig. 8(h)]. We see clearly that the HOM results are close to ideal near the image center but poorer near the edges. To obtain these images from 500 couples of experimental images, we removed the random noise by first binning the pixels 4×4 and second convolving the mean correlation image with a Gaussian kernel, whose integral corresponds to 44 binned pixels. Theses operations induce a strong loss of resolution but are necessary to obtain reliable maps with 500 image pairs. In the Appendix, we present a calculation that shows that the chosen resolution ensures a sufficient signal-to-noise ratio in the images of Fig. 8.

IV. CONCLUSION

We have reported the first experimental observation of fully spatiotemporal HOM interference of biphoton states of extremely high Schmidt number. Two-photon interference of 1500 spatial modes and more than 3×10^6 spatiotemporal modes is evidenced by measuring

momentum spatial coincidences between pixels of far-field images of two SPDC beams propagating through a HOM interferometer. The output beams are detected with two separate detector arrays operating in the photon-counting regime. The properties of HOM interference are investigated in both the time and space domains. We show that the two-photon interference exhibits temporal and 2D spatial HOM dips with an average visibility of 60% and widths in good agreement with the spatiotemporal coherence properties of the biphoton state and the geometry of the HOM interferometer. This relatively low visibility, compared to the expected value, is probably due to geometric aberrations of the imaging system. Moreover, we also demonstrate that, using detectors arrays, 2D momentum spatial coincidences are resolved between the two output ports as well as within the two single-port images. This method gives us access to the rates and the 2D momentum correlation distributions of twin photons detected in pairs between the two cameras and on each camera. We also emphasize that the temporal coherence of the biphoton state is measured with detectors that record spatial coincidences on the whole set of photons, without any prior selection of the photons in time and space coincidence. Given the critical role played by two-photon HOM interferences in most quantum information and quantum technology schemes, our demonstration that HOM interference can be obtained by manipulating a very-high-dimensional entangled state paves the way to very-high-dimensional quantum information schemes using space and time variables. For example, the teleportation protocol of Bouwmeester *et al.* [16] used a HOM setup to perform the discrimination of the Bell states. Hence, our experiment paves the way to the teleportation of images, despite the fact that it can be proven [30] that a purely linear system cannot be used to teleport a qudit, where the d of qudit means a dimension greater than 2. Nevertheless, a teleportation of a qutrit has recently been reported [31] by using ancilla photons and a supplementary dimension. Further investigation is necessary to understand how to master spatial aspects of HOM interference in such types of protocols. Because some cryptography protocols use teleportation, applications to cryptography in multimode fibers could follow. Another application concerns communications in quantum computing [32].

ACKNOWLEDGMENTS

This work was partly supported by the French "Investissements d'Avenir" program, Project ISITE-BFC (Contract No. ANR-15-IDEX-03).

APPENDIX: SIGNAL-TO-NOISE RATIO ESTIMATION

In this Appendix, we calculate the signal-to-noise ratio obtained in the images of Fig. 8, first obtained by averaging 500 experimental images and then binning the pixels 4×4 and convolving the binned image by a Gaussian kernel. Hence, the resolution cell in the 256×256-pixel images of Fig. 8 contains $P = 23 \times 23$ pixels.

On each image, the threshold number of photons, 0 or 1, follows a Bernouilli law of mean m (here, $m = 0.12$) and of variance $m(1-m)$. For independent images, the true covariance vanishes, but the estimator of covariance experiences fluctuations. If we use N images and P pixels in each image, which can be considered independent in this calculation, the variance V of this estimator is given by $V = [m^2 \times (1-m^2)/NP]$. For $m = 0.12$ photon/pixel, $N = 500$ images, and $P = 23 \times 23$ pixels, we obtain a standard deviation $V^{1/2} = 2.31 \times 10^{-4}$ photon/pixel.

On the other hand, the twin signal t can be estimated as $t = (m/P') \times 13\% = 5.8 \times 10^{-4}$ photon/pixel, where 13% is the ratio in C_{12} given above and $P' = 27$ pixels is the normalized integral of the correlation peak. By binning the pixels 4×4, this signal is, experimentally, multiplied by 10 because of the partial correlation between neighbor pixels, while the standard deviation of the covariance is only multiplied by 4 (see above, P divided by 16). This process gives a signal-to-noise ratio of approximately 6 for the twin signal [Fig. 8(c)] and of 3 for the HOM signal [Fig. 8(f)]. These results are the minimum ratios needed to observe a clear spatially deterministic signal in the HOM signal, which allows a first experimental map of its quality but with a resolution that needs to be improved.

[1] G. Lubin, R. Tenne, I. M. Antolovic, E. Charbon, C. Bruschini, and D. Oron, *Quantum Correlation Measurement with Single Photon Avalanche Diode Arrays*, Opt. Express **27**, 32863 (2019).

[2] P.-A. Moreau, E. Toninelli, T. Gregory, and M. J. Padgett, *Imaging with Quantum States of Light*, Nat. Rev. Phys. **1**, 367 (2019).

[3] P.-A. Moreau, J. Mougin-Sisini, F. Devaux, and E. Lantz, *Realization of the Purely Spatial Einstein-Podolsky-Rosen Paradox in Full-Field Images of Spontaneous Parametric Down-Conversion*, Phys. Rev. A **86**, 010101(R) (2012).

[4] P.-A. Moreau, F. Devaux, and E. Lantz, *Einstein-Podolsky-Rosen Paradox in Twin Images*, Phys. Rev. Lett. **113**, 160401 (2014).

[5] E. Lantz, S. Denis, P.-A. Moreau, and F. Devaux, *Einstein-Podolsky-Rosen Paradox in Single Pairs of Images*, Opt. Express **23**, 26472 (2015).

[6] M. P. Edgar, D. S. Tasca, F. Izdebski, R. E. Warburton, J. Leach, M. Agnew, G. S. Buller, R. W. Boyd, and M. J. Padgett, *Imaging High-Dimensional Spatial Entanglement with a Camera*, Nat. Commun. **3**, 984 (2012).

[7] P. A. Morris, R. S. Aspden, J. E. C. Bell, R. W. Boyd, and M. J. Padgett, *Imaging with a Small Number of Photons*, Nat. Commun. **6**, 5913 (2015).

[8] S. Denis, P.-A. Moreau, F. Devaux, and E. Lantz, *Temporal Ghost Imaging with Twin Photons*, J. Opt. **19**, 034002 (2017).

[9] H. Defienne, M. Reichert, and J. W. Fleischer, *Adaptive Quantum Optics with Spatially Entangled Photon Pairs*, Phys. Rev. Lett. **121**, 233601 (2018).

[10] F. Devaux, A. Mosset, F. Bassignot, and E. Lantz, *Quantum Holography with Biphotons of High Schmidt Number*, Phys. Rev. A **99**, 033854 (2019).

[11] G. Brida, M. Genovese, and I. R. Berchera, *Experimental Realization of Sub-Shot-Noise Quantum Imaging*, Nat. Photonics **4**, 227 (2010).

[12] E. Toninelli, M. P. Edgar, P.-A. Moreau, G. M. Gibson, G. D. Hammond, and M. J. Padgett, *Sub-Shot-Noise Shadow Sensing with Quantum Correlations*, Opt. Express **25**, 21826 (2017).

[13] G. B. Lemos, V. Borish, G. D. Cole, S. Ramelow, R. Lapkiewicz, and A. Zeilinger, *Quantum Imaging with Undetected Photons*, Nature (London) **512**, 409 (2014).

[14] C. K. Hong, Z. Y. Ou, and L. Mandel, *Measurement of Subpicosecond Time Intervals between Two Photons by Interference*, Phys. Rev. Lett. **59**, 2044 (1987).

[15] D. S. Simon, G. Jaeger, and A. V. Sergienko, *Quantum Metrology, Imaging, and Communication*, *Quantum Science and Technology* (Springer International, New York, 2017).

[16] D. Bouwmeester, J.-W. Pan, K. Mattle, M. Eibl, H. Weinfurter, and A. Zeilinger, *Experimental Quantum Teleportation*, Nature (London) **390**, 575 (1997).

[17] P. Kok, W. J. Munro, K. Nemoto, T. C. Ralph, J. P. Dowling, and G. J. Milburn, *Linear Optical Quantum Computing with Photonic Qubits*, Rev. Mod. Phys. **79**, 135 (2007).

[18] B. T. Gard, K. R. Motes, J. P. Olson, P. P. Rohde, and J. P. Dowling, in *From Atomic to Mesoscale* (World Scientific, Singapore, 2015), pp. 167–192.

[19] Y.-H. Deng, H. Wang, X. Ding, Z.-C. Duan, J. Qin, M.-C. Chen, Y. He, Y.-M. He, J.-P. Li, Y.-H. Li *et al.*, *Quantum Interference between Light Sources Separated by 150 Million Kilometers*, Phys. Rev. Lett. **123**, 080401 (2019).

[20] P. S. K. Lee and M. P. van Exter, *Spatial Labeling in a Two-Photon Interferometer*, Phys. Rev. A **73**, 063827 (2006).

[21] M. Jachura and R. Chrapkiewicz, *Shot-by-Shot Imaging of Hong-Ou-Mandel Interference with an Intensified sCMOS Camera*, Opt. Lett. **40**, 1540 (2015).

[22] R. Chrapkiewicz, M. Jachura, K. Banaszek, and W. Wasilewski, *Hologram of a Single Photon*, Nat. Photonics **10**, 576 (2016).

[23] Z. Y. Ou and L. Mandel, *Further Evidence of Nonclassical Behavior in Optical Interference*, Phys. Rev. Lett. **62**, 2941 (1989).

[24] H. Kim, O. Kwon, W. Kim, and T. Kim, *Spatial Two-Photon Interference in a Hong-Ou-Mandel Interferometer*, Phys. Rev. A **73**, 023820 (2006).

[25] S. P. Walborn, A. N. de Oliveira, S. Pádua, and C. H. Monken, *Multimode Hong-Ou-Mandel Interference*, Phys. Rev. Lett. **90**, 143601 (2003).

[26] H. Di Lorenzo Pires, H. C. B. Florijn, and M. P. van Exter, *Measurement of the Spiral Spectrum of Entangled Two-Photon States*, Phys. Rev. Lett. **104**, 020505 (2010).

[27] F. Devaux, A. Mosset, and E. Lantz, *Stochastic Numerical Simulations of a Fully Spatiotemporal Hong-Ou-Mandel Dip*, Phys. Rev. A **100**, 013845 (2019).

[28] E. Lantz, J.-L. Blanchet, L. Furfaro, and F. Devaux, *Multi-imaging and Bayesian Estimation for Photon Counting with EMCCDs*, Mon. Not. R. Astron. Soc. **386**, 2262 (2008).

[29] C. K. Law and J. H. Eberly, *Analysis and Interpretation of High Transverse Entanglement in Optical Parametric Down Conversion*, Phys. Rev. Lett. **92**, 127903 (2004).

[30] J. Calsamiglia, *Generalized Measurements by Linear Elements*, Phys. Rev. A **65**, 030301(R) (2002).

[31] Y.-H. Luo, H.-S. Zhong, M. Erhard, X.-L. Wang, L.-C. Peng, M. Krenn, X. Jiang, L. Li, N.-L. Liu, and C.-Y. Lu, *Quantum Teleportation in High Dimensions*, Phys. Rev. Lett. **123**, 070505 (2019).

[32] D. Llewellyn, Y. Ding, I. I. Faruque, S. Paesani, D. Bacco, R. Santagati, Y. Qian, Y. Li, Y. Xiao, M. Huber, M. Malik, G. F. Sinclair, X. Zhou, K. Rottwitt, J. L. O'Brien, J. G. Rarity, Q. Gong, L. K. Oxenlowe, J. Wang, and M. G. Thompson, *Chip-to-Chip Quantum Teleportation and Multi-photon Entanglement in Silicon*, Nat. Phys. **16**, 148 (2020).